RESEARCH ARTICLE
SOLID EARTH: GEODYNAMICS

Earth and Planetary Physics
6: 191–203, 2022
doi: 10.26464/epp2022016

Numerical modeling of metamorphic core complex formation: Implications for the destruction of the North China Craton

ZiQi Ma[1,2], Gang Lu[1*], JianFeng Yang[1], and Liang Zhao[1,2]

[1]State Key Laboratory of Lithospheric Evolution, Institute of Geology and Geophysics, Chinese Academy of Sciences, Beijing 100029, China;

[2]College of Earth and Planetary Sciences, University of Chinese Academy of Sciences, Beijing 100049, China

Citation: Ma, Z. Q., Lu, G., Yang, J. F., and Zhao, L. (2022). Numerical modeling of metamorphic core complex formation: Implications for the destruction of the North China Craton. *Earth Planet. Phys.*, *6*(2), 191–203. http://doi.org/10.26464/epp2022016

Abstract: Widespread magmatism, metamorphic core complexes (MCCs), and significant lithospheric thinning occurred during the Mesozoic in the North China Craton (NCC). It has been suggested that the coeval exhumation of MCCs with uniform northwest-southeast shear senses and magmatism probably resulted from a decratonization event during the retreat of the paleo-Pacific Plate. Here we used two-dimensional finite element thermomechanical numerical models to investigate critical parameters controlling the formation of MCCs under far-field extensional stress. We observed three end-member deformation modes: the MCC mode, the symmetric-dome mode, and the pure-shear mode. The MCC mode requires a Moho temperature of ≥700 °C and an extensional strain rate of $\geq 5 \times 10^{-16}$ s^{-1}, implying that the lithosphere had already thinned when the MCC was formed in the Mesozoic. Considering that the widespread MCCs have the same northwest-southeast extension direction in the NCC, we suggest that the MCCs are surface expressions of both large-scale extension and craton destruction and that rollback of the paleo-Pacific slab might be the common driving force.

Keywords: metamorphic core complex; North China Craton; numerical modeling; extension

1. Introduction

A metamorphic core complex (MCC) is a domal or arched structure characterized by three main features (Whitney et al., 2013; Platt et al., 2015; Brun et al., 2018; Lin W and Wei W, 2020): (1) a large-offset, low-angle (<30°) detachment fault, (2) direct contact of the brittle upper crust and ductile lower crust, and (3) a domal structure of the metamorphic core exhumed at the surface. Since their identification in the Cordillera (Davis and Coney, 1979; Coney, 1980), MCCs have quickly captured geologists' attention because the significantly low-angle normal fault violates the classical Anderson fault theory (Anderson, 1951), which predicts that normal faults form at high angles (>45°) under extension. Because the exhumation of the mid-lower crust could carry information on the deep crust, MCCs are generally acknowledged as a surface response of deep tectonic processes (Davis and Coney, 1979; Coney and Harms, 1984; Lister et al., 1984). As an indicator of large-offset extension, MCCs have been widely identified in many extensional locations, including the Basin and Range Province in the United States (Davis and Coney, 1979; Wernicke, 1981; Coney and Harms, 1984) and the Cyclades in the Aegean Sea (Lister et al., 1984).

Intensive studies have been done to explore the mechanisms and conditions of MCC formation, including field observations (Coney and Harms, 1984; Lister and Davis, 1989; Lin W and Wei W, 2020), analogue simulations (Brun et al., 1994, 2018; Brun, 1999; Tirel et al., 2006), and numerical simulations (Lavier et al., 1999; Tirel et al., 2004, 2008; Wijns et al., 2005; Rey et al., 2009a, b; Huet et al., 2011; Le Pourhiet et al., 2012; Schenker et al., 2012; Wang K et al., 2015; Lu G et al., 2016; Wu GL and Lavier, 2016). Various factors responsible for MCC formation have been proposed: (1) strain localization that accounts for the low-angle deflection of the detachment fault (Lavier et al., 1999, 2000); (2) a temperature rise and partial melting (Buck, 1991; Tirel et al., 2008; Rey et al., 2009a, b; Wang K et al., 2015); (3) a thickened crust (Buck, 1991; Tirel et al., 2008); and (4) a contrasting viscosity structure between the strong upper crust and the relatively weak lower crust (Lu G et al., 2016). However, the kinematics, timing, and formation mechanism of MCCs are still under debate. Some have supported the idea that a temperature rise and partial melting promote the formation of an MCC (Buck, 1991; Lavier and Buck, 2002; Tirel et al., 2004, 2008; Rey et al., 2009a, b; Schenker et al., 2012; Wang K et al., 2015), whereas Huet et al. (2011) argued that high temperature is not a prerequisite. Most MCCs are found in the orogen; therefore, the formation of an MCC is classically attributed to post-orogenic collapse by a thickened crust (Buck, 1991; Tirel et al., 2008). However, recent numerical models have shown that MCCs can still form without a thickened crust (Wang K et al., 2015), undermining the post-orogenic collapse theory to a certain extent.

Cratons are long-term stable terrane units on Earth that lack tectonic and magmatic activities over billions of years. However, the North China Craton (NCC) is abnormal in that it has undergone

Correspondence to: G. Lu, lvgang@mail.iggcas.ac.cn
Received 15 OCT 2021; Accepted 29 DEC 2021.
Accepted article online 27 JAN 2022.

significant lithospheric thinning and destruction (Wu FY et al., 2008, 2019; Zhu RX et al., 2011, 2020; Zhu RX and Xu YG, 2019). Observed diamond-bearing kimberlites at Mengyin, Tieling, and Fuxian in the NCC have demonstrated that the NCC was once ~200 km thick in the middle Ordovician (Zhu RX and Zheng TY, 2009). Studies of peridotite enclaves and mineral inclusions in diamond from kimberlite have shown that the surface heat flux of the NCC in the Paleozoic was 40 mW/m^2 (Griffin et al., 1998; Xu YG, 2001), a typical value for stable cratons. In contrast, geochemical and geophysical observations have revealed a thinned lithosphere and a high surface heat flux in the eastern NCC (Griffin et al., 1998; Hu SB et al., 2000; Menzies et al., 2007; Chen L, 2010).

The widespread distribution of MCCs sharing a consistent northwest–southeast shear sense in the NCC occurred in a narrow age range (120–130 Ma) contemporarily with the destruction of the craton, indicating an intimate relationship between MCC formation and the craton destruction event. Here we used numerical models to investigate crucial parameters controlling the formation of an MCC and further constrain the factors that triggered craton destruction.

2. Geological Setting

The NCC is one of the oldest cratonic blocks globally, containing Archean rocks as old as 3.8 Ga (Liu DY et al., 1992). It is bounded to the north by the Central Asian Orogenic Belt and to the south by the Qinling–Dabie–Sulu Orogenic Belt (Wang HZ and Mo XX, 1995; Figure 1a). The NCC consists of two major blocks, the western NCC and the eastern NCC, separated by the Trans-North China Orogen (TNCO; Zhao GC et al., 2005). After assembling the western and the eastern blocks along this orogen during the Paleoproterozoic (~1.9–1.85 Ga; Zhao GC et al., 2005), the NCC finalized its cratonization and remained stable until the Mesozoic. In the Mesozoic, the eastern block underwent significant lithospheric thinning and destruction (Wu FY et al., 2019; Zhu RX and Xu YG, 2019; Zhu RX et al., 2020). Seismic observations have shown that the current NCC has crustal thicknesses of ~30 km in the destructed eastern block and ~40 km in the stable western block (Chen L et al., 2006; Zheng TY et al., 2006; Bao XW et al., 2015; Wei ZG et al., 2015; Xia B et al., 2017; Zheng TY et al., 2017).

The NCC experienced several tectonic events during the Late Mesozoic. During the Early Triassic, the closure of the paleo-Asian ocean (along the Xing'an Mongolian Orogenic Belt, the eastern part of the Central Asian Orogenic Belt) in the north and the Dabie–Sulu Ocean in the south resulted in the NCC forming part of the East Asian continent (Wang HZ and Mo XX, 1995). The paleo-Pacific subduction beneath the East Asian continent began in the Jurassic to the east of the NCC (Wang HZ and Mo XX, 1995). Field data have suggested that the NCC experienced two compressional events, one in the Middle Jurassic and the other in the Early Cretaceous, and two major extension periods, one in the Late Jurassic and the other after the compressional event in the Early Cretaceous (Zhu RX and Xu YG, 2019; Zhu RX et al., 2020).

The extension in the Early Cretaceous was intensive, accompanied by the development of widespread volcanic eruptions, granitic intrusions, and related gold mineralization (Wang HZ and Mo XX, 1995; Wu FY et al., 2008, 2019; Zhu RX and Xu YG, 2019). Three peaks of magmatism occurred in the Triassic, Jurassic, and Early Cretaceous (Figure 1c). Metamorphic core complexes are widely distributed in the NCC (Figure 1a), from the Hohhot MCC (Davis et al., 2002; Lin W and Wang QC, 2006) in the northwest to the Yunmeng Mountain MCC (Zheng YD et al., 1988; Davis et al., 2002; Lin W and Wang QC, 2006; Chen Y et al., 2014) in the central NCC, to the eastern Yiwulu Mountain (Waziyu) MCC (Darby et al., 2004; Zhang BL et al., 2012) and southern Liaoning MCC (Liu JL et al., 2005, 2013; Ji M et al., 2015) in the east, and the Xiaoqinling MCC (Zhang JJ and Zheng YD, 1999; Li YJ et al., 2020; Lin W and Wei W, 2020) at the south margin. It is noteworthy that MCCs in the NCC have the following common characteristics: (1) they have similar activity times (135–115 Ma; Figures 1c and 1d), and (2) they have similar shear sense directions (northwest-southeast; Figure 1a). These characteristics suggest that the formation of MCCs may be controlled by a common large-scale tectonic stress and linked to a change in the thermal state of the lithosphere. In this study, we used two-dimensional (2-D) thermomechanical numerical experiments to investigate MCC formation under the boundary extension and explore the effects of two controlling factors, strain rate and Moho temperature, on MCC formation.

3. Method

3.1 Governing Equations

We used the 2-D thermomechanical finite-element code MILAMIN_VEP2 (Kaus, 2010; Thielmann and Kaus, 2012) to simulate incompressible viscoplastic flow. The code solves the mass, momentum, and energy conservation equations of incompressible flow under the general Boussinesq approximation:

$$\frac{\partial v_i}{\partial x_i} = 0, \tag{1}$$

$$-\frac{\partial P}{\partial x_i} + \frac{\partial \tau_{ij}}{\partial x_j} + \rho g_i = 0, \tag{2}$$

$$\rho c_p \left(\frac{\partial T}{\partial t} + v_i \frac{\partial T}{\partial x_i} \right) = \frac{\partial}{\partial x_i} \left(k \frac{\partial T}{\partial x_i} \right) + H_r, \tag{3}$$

where $x_{i,j}$ represent spatial coordinates, $v_{i,j}$ are components of velocity, and repeated indices are summed. Variables P, ρ, g, c_p, T, t, and k denote pressure, density, gravitational acceleration, heat capacity, temperature, time, and thermal conductivity, respectively. In addition, $\tau_{ij} = 2\eta\dot{\varepsilon}_{ij}$ is the deviatoric stress, where $\dot{\varepsilon}_{ij} = \frac{1}{2}\left(\frac{\partial v_i}{\partial x_j} + \frac{\partial v_j}{\partial x_i}\right)$ is the strain rate tensor; $H_s = \tau_{ij}\dot{\varepsilon}_{ij}$ is shear heating; and H_r is radioactive heat.

The rheology is assumed to be viscoplastic. The total strain rate is given by

$$\dot{\varepsilon}_{ij} = \dot{\varepsilon}_{ij}^{\mathrm{vis}} + \dot{\varepsilon}_{ij}^{\mathrm{pl}} = \frac{1}{2\eta_{\mathrm{eff}}}\tau_{ij} + \dot{\lambda}\frac{\partial Q}{\partial \sigma_{ij}}, \tag{4}$$

where $\dot{\varepsilon}_{ij}^{\mathrm{vis}}$ and $\dot{\varepsilon}_{ij}^{\mathrm{pl}}$ represent the viscous and plastic strain rate, respectively, $\dot{\lambda}$ denotes the plastic multiplier, and Q is the corresponding plastic flow potential (Kaus, 2010).

A laboratory-based temperature and the strain rate-dependent dislocation creep flow law were used, with the effective viscosity

(η_{eff}) given by

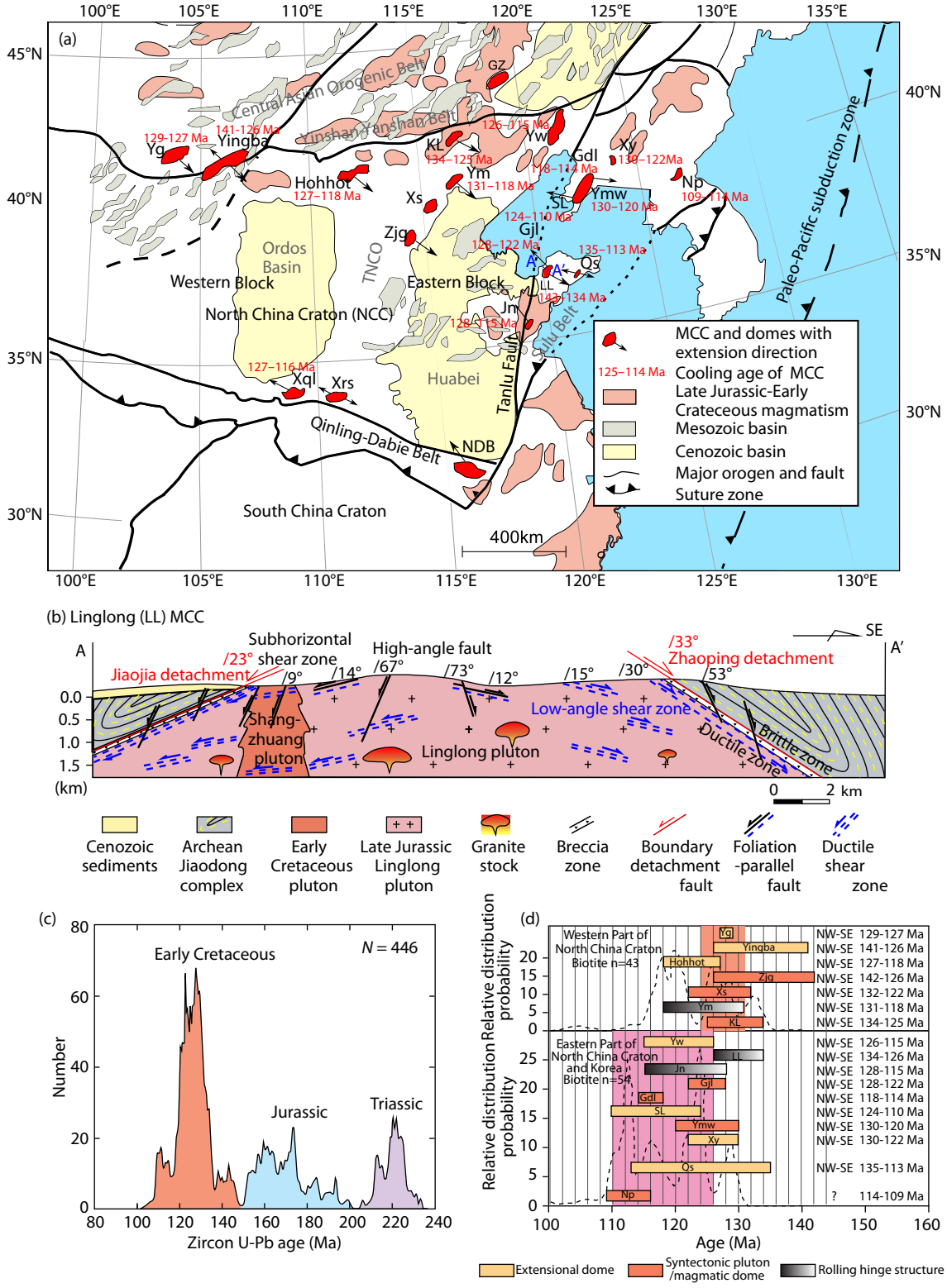

Figure 1. (a) Distribution of Mesozoic metamorphic core complexes (MCCs) and domes in the North China Craton (NCC). Numbers in red indicate MCC ages, and arrows indicate their shear senses. TNCO, Trans-North China Orogen. MCC code: Gdl, Gudaoling magmatic dome; Gjl, Guojialing syn-tectonic granite; GZ, Ganzhuermiao; Jn, southern Shandong extensive dome; KL, Kalaqin; LL, Linglong; NDB, North Dabie; Np, Nampho magmatic dome; Qs, Queshan; SL, Southern Liaoning; Xql, Xiaoqinling; Xrs, Xiongershan; Xs, Xishan; Xy, Xiuyan; Ymw, Yimawanshan magmatic domes; Yg, Yagan; Ym, Yunmeng Mountain; Yw, Yiwulu Mountain; Zjg, Zijingguan. Modified from Wang T et al. (2011). (b) Cross-section of the Linglong MCC (modified from Wu XD et al., 2020). (c) Zircon U-Pb ages of Mesozoic igneous rocks in the NCC showing three magmatic peaks in this area (modified from Wu FY et al., 2019). (d) Ages of extensional structures in the NCC (modified from Lin W and Wei W, 2020).

$$\eta_{\text{eff}} = \frac{1}{2} f F A_D^{-\frac{1}{n}} \dot{\varepsilon}_{II}^{\frac{1}{n}-1} \exp\left(\frac{E+PV}{nRT}\right), \tag{5}$$

where $F = \frac{1}{2^{\frac{n-1}{n}} 3^{\frac{n+1}{2n}}}$ is the experiment correction factor, R is the ideal gas constant (8.314 J/K/mol), A_D is the pre-exponential factor, n is the stress exponent, E is the activation energy, V is the activation volume (Table 1), $\dot{\varepsilon}_{\text{II}} = \sqrt{0.5\dot{\varepsilon}_{ij}\dot{\varepsilon}_{ij}}$ is the second invariant of the strain rate tensor, and f is a viscosity scaling factor that represents stronger or weaker materials.

When the stress exceeds the yield stress of the rock, the rock undergoes plastic failure. The yield stress is based on the Drucker–Prager fracture criterion:

$$\tau_y = \tau_{2\text{nd}} = P\sin\varphi + C\cos\varphi, \tag{6}$$

where $\tau_{2\text{nd}} = \sqrt{0.5\tau_{ij}\tau_{ij}}$ is the second invariant of the deviatoric stress, C is the cohesion, and φ is the frictional angle. Rocks are subject to damage after yielding, parameterized by a linear reduction of cohesion C and the internal friction angle φ between a plastic strain of 0.1 to 1.5 (Figure 2e; Lavier and Buck, 2002; Wang K et al., 2015). We also took into account plastic healing (Püthe and Gerya, 2014) with a rate of $\dot{\varepsilon}_{\text{healing}} = 1 \times 10^{-15}$ s^{-1}. Details of the model parameters are shown in Table 1.

3.2 Steady-State Geotherm of Old Lithosphere

Radioactive elements such as uranium and thorium are incompatible components enriched in the crust and depleted in the mantle. Therefore, it is reasonable to assume that the radioactive heat in the lithospheric mantle approaches zero. When the heat lost by the crust balances the heat gained, with fixed heat production from radioactive heat in the lithosphere, a steady state is reached. We assumed that the old continental lithosphere reached a steady state (McKenzie et al., 2005); thus, Equation (3) turns into

$$k\frac{\partial^2 T}{\partial z^2} + H_r = 0, \tag{7}$$

where k is thermal conductivity, T denotes the temperature, z is the depth, and H_r is the radioactive heat.

In the crust, Equation (7) leads to an analytical solution of the temperature that increases with depth (Figure 2b) in the form of

$$T = T_0 - \frac{H_r}{2k}(z - z_m)z + \frac{T_{\text{Moho}}}{z_m}z, \tag{8}$$

where T_0 denotes the surface temperature, T_{Moho} is the Moho temperature, and z_m is the Moho depth.

Because heat generation within the mantle is taken to be zero, and thus the steady-state heat flux through the entire lithosphere is continuous, the thermal gradient in the lithospheric mantle equals the thermal gradient in the crust at the Moho:

$$\left.\frac{\mathrm{d}T}{\mathrm{d}z}\right|_{\text{Moho}} = -\frac{H_r z_m}{2k} + \frac{T_{\text{Moho}}}{z_m}. \tag{9}$$

The depth of the thermal lithosphere–asthenosphere boundary (LAB) is thus

Table 1. Model parameters used in the reference model.

Parameter	Symbol	Unit	Upper crust	Lower crust
Thickness	h	km	20	20
Density	ρ	kg m^{-3}	2,700	2,800
Radioactive heat	H_r	W m^{-3}	9×10^{-7}	9×10^{-7}
Thermal conductivity	k	W m^{-1} K^{-1}	2.5	2.5
Heat capacity	c_p	J kg K^{-1}	1,050	1,050
Flow law	—	—	Dry granite[a]	Diabase[a]
Stress exponent	n	—	3.3	3
Viscosity scaling factor	f	—	10	0.1
Prefactor	A_D	s^{-1} Pa^{-n}	3.16×10^{-26}	3.2×10^{-20}
Activation energy	E	kJ mol^{-1}	190	276
Activation volume	V	m^3 mol^{-1}	0	0
Plastic strain healing rate	$\dot{\varepsilon}_{\text{healing}}$	s^{-1}	1×10^{-15}	1×10^{-15}
Frictional angle	φ	°	30–3	30–3
Cohesion	C	MPa	20–2	20–2
Strain range for weakening	ε_p	—	0.1–1.5	0.1–1.5
Surface temperature	T_0	°C	0	0
Bottom temperature	T_{Moho}	°C	750	750
Background strain rate	$\dot{\varepsilon}_{\text{bg}}$	s^{-1}	5×10^{-16}	5×10^{-16}

[a]Parameters are taken from Schmalholz et al. (2009).

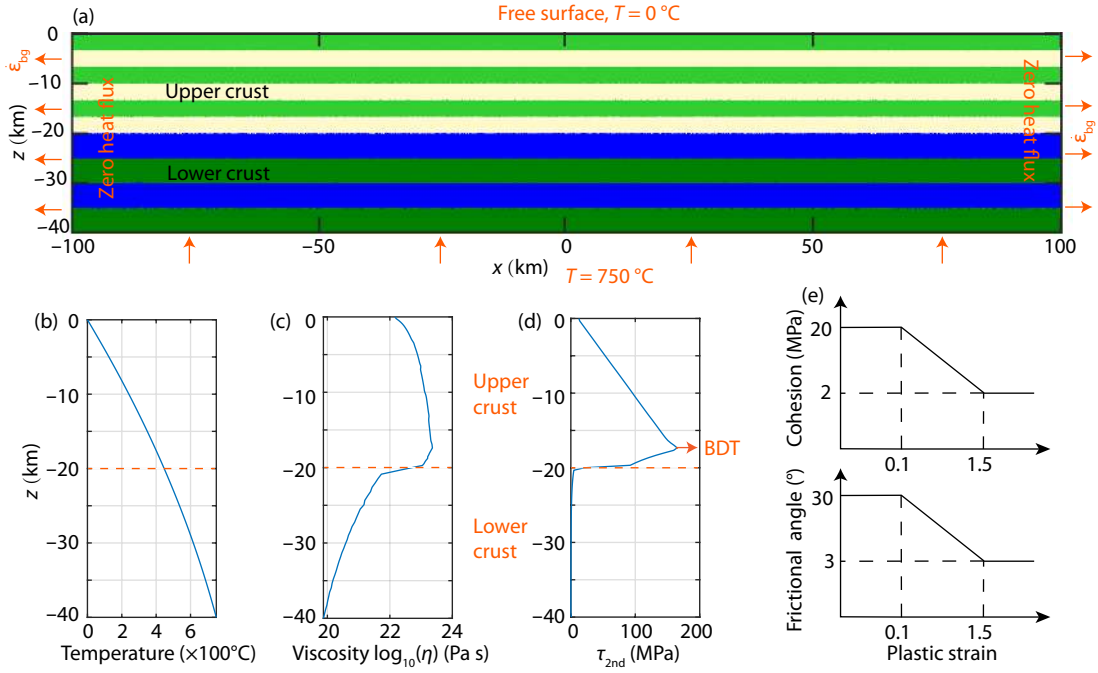

Figure 2. Model setup. (a) The 2-D model domain (40 × 200 km) with composition field and boundary conditions. (b–d) Profiles of temperature (b), viscosity (c), and strength (d) at a background strain rate of 5×10^{-16} s^{-1} of the reference model. (e) The linear strain weakening mechanism. BDT, brittle–ductile transition.

$$z_{\mathrm{LAB}} = z_m + \frac{T_{\mathrm{LAB}} - T_{\mathrm{Moho}}}{\mathrm{d}T/\mathrm{d}z}, \tag{10}$$

where T_{LAB} is the temperature at the base of the lithosphere.

3.3 Model Setup

We assumed that the destructed eastern block initially had the same crustal thickness as the stable western block, ~40 km at present, constrained by the receiver function observation (Chen L et al., 2006). Following previous studies (Wijns et al., 2005; Gessner et al., 2007; Lu G et al., 2016), we set the model to 200 km wide and 40 km deep (Figure 2a), consisting of two horizontal layers representing the upper crust (20 km) and the lower crust (20 km). The model was discretized with 451 × 121 evenly distributed grids in the horizontal and vertical directions, respectively. The model had an impermeable lower boundary, which allowed us to study the formation of MCCs with a relatively flat Moho (Tirel et al., 2008; Schenker et al., 2012; Wang K et al., 2015).

The top boundary was a free surface, and a free-surface stabilization algorithm was implemented (Kaus et al., 2010). Side boundaries were extended at a constant background strain rate ($\dot{\varepsilon}_{\mathrm{bg}}$), whereas a return strain rate ($-\dot{\varepsilon}_{\mathrm{bg}}$) was applied at the bottom boundary to ensure mass conservation. Constant-temperature boundary conditions were adopted for the top and bottom boundaries, which for the reference model were T_0 = 0 °C and T_{Moho} = 750 °C. Side boundaries had zero heat flux.

4. Results

We performed 20 models with varying background strain rates ($\dot{\varepsilon}_{\mathrm{bg}}$) and Moho temperatures (T_{Moho}; Table 2). All models were terminated when the crustal thickness was reduced to 30 km, consistent with the present-day crustal thickness in the eastern NCC (Chen L et al., 2006; Bao XW et al., 2015; Wei ZG et al., 2015; Xia B et al., 2017). Three end-member deformation modes were observed: (1) the MCC mode, characterized by the formation of a low-angle detachment fault and rapid exhumation of the lower crust material; (2) the symmetric-dome mode, characterized by a slow uplift of the lower crustal material without a detachment fault; and (3) the pure-shear mode, with uniform crustal extension. Below we describe the three end-member modes in detail.

4.1 Reference MCC Mode

The reference model E5T750, with a background extension strain rate of $\dot{\varepsilon}_{\mathrm{bg}} = 5 \times 10^{-16}$ s^{-1} and a Moho temperature of T_{Moho} = 750 °C, evolved as a "rolling-hinge" MCC mode (Figure 3). At the early stage (13% of extension), two pairs of conjugated high-strain-rate shear zones formed with high angles (>45°) in the brittle upper crust, leading to the formation of two necking centers in the upper crust (Figure 3a). Deformation became more concentrated at 16% of extension (Figure 3b). In both necking centers, the right limb of the conjugated shear zones became inactive, leading to the formation of asymmetric shear zones. At this stage, the faults remained at a high angle (49°). At 19% of extension, deformation became further concentrated at the asymmetric shear zone in the right necking center, whereas the left necking center became inactive (Figure 3c). With ongoing extension, the strain rate continued to localize strongly at the asymmetric fault in the right necking center. New faults appeared in the deep dip at 36°, whereas old faults began rotating gradually to lower angles as they approached the surface. The fault near the surface had a low angle

Table 2. Description of the numerical experiments and modes of deformation.

Model no.	$\dot{\varepsilon}_{bg}$ (10^{-16} s^{-1})	T_{Moho} (°C)	Fault angle[a] (°)	Mode
E05T600	0.5	600	–	Symmetric dome
E05T650	0.5	650	–	Symmetric dome
E05T700	0.5	700	–	Symmetric dome
E05T750	0.5	750	–	Symmetric dome
E05T800	0.5	800	–	Symmetric dome
E1T600	1	600	–	Symmetric dome
E1T650	1	650	–	Symmetric dome
E1T700	1	700	–	Symmetric dome
E1T750	1	750	16–20	MCC
E1T800	1	800	17–20	MCC
E5T600	5	600	–	Pure shear
E5T650	5	650	–	Symmetric dome
E5T700	5	700	13–26	MCC
E5T750	5	750	10–21	MCC
E5T800	5	800	10–23	MCC
E10T600	10	600	–	Pure shear
E10T650	10	650	–	Pure shear
E10T700	10	700	19–58	MCC
E10T750	10	750	14–28	MCC
E10T800	10	800	16–27	MCC

[a]Fault angle was measured at a depth of 0–4 km on those faults where strain localization occurred, and strain rate was locally larger than 1×10^{-14} s^{-1} at a total extension of 33%.

of 18°. As a result, the lower crustal material on the footwall of the active faults was exhumed along the detachment fault. Upwelling of the ductile lower crust caused by the local pressure gradient resulting from upper crustal necking "pushed" the detachment fault upward, resulting in rotation of the detachment fault and formation of the MCC, which was comparable to the "rolling hinge" mode (Axen and Hartley, 1997; Wu GL et al., 2015). Finally, at 33% of extension (Figure 3d), the lower crust was exhumed to the surface, and the dip angle of the minimum detachment fault decreased to 10°. The *P-T-t* paths show that within 18 Myr, both the pressure (from ~0.8 to ~0.1 GPa) and the temperature (from ~620 to ~100 °C) essentially dropped. The stress profile showed that the surrounding upper crust sustained considerable stress of ~140 MPa, whereas the lower crust was weak, with low stress.

4.2 Symmetric-Dome Mode

Model E1T700, which had boundary conditions of $\dot{\varepsilon}_{bg}= 1 \times 10^{-16}$ s^{-1} and T_{Moho} = 700 °C, evolved in the symmetric-dome mode. At the early stage (11% of extension), the model underwent similar deformation as the reference model, forming two pairs of conjugated shear zones, and as a result, two necking centers in the upper crust (Figure 4a). The conjugate faults were all at high angles (>50°). However, the strain rate was less concentrated in the shear zones than in the reference model. With further extension, unlike in the reference model, the conjugate shear zones did not evolve into asymmetric shear zones. Instead, both necking centers remained active, and the conjugate shear zones became more diffused (Figure 4b). Dips of the active shear zones remained high, and no low-angle detachment fault formed. The upper crust continued to neck, and the weak lower crust slowly exhumed upward to form symmetric domes. Tracers of the *P-T-t* paths demonstrated a total cooling of nearly 300 °C over a relatively long time (90 Myr), which yielded a cooling rate of ~3 °C/Myr. Compared with the MCC mode, the symmetric-dome mode also experienced cooling and decompression, but the duration was much longer. The stress profile showed a similar pattern (a strong upper crust with ~150 MPa stress and a weak lower crust) as the MCC mode.

4.3 Pure-Shear Mode

Model E5T600, which had $\dot{\varepsilon}_{bg}= 5 \times 10^{-16}$ s^{-1} and T_{Moho} = 600 °C, evolved in a pure-shear mode (Figure 5). The crust was uniformly thinned to 30 km in a pure-shear style, with distributed deformation in the entire model domain. Although there were several necking zones in the crust, there was insufficient shear localization to develop conjugated shear zones (Figure 5a). As a result, we defined those cases as the pure-shear mode. The tracers experienced little decompression and cooling in this case.

4.4 Conditions of MCC Formation

To constrain the conditions of MCC formation, we performed systematic runs with varied Moho temperatures and extension strain rates. Our results indicated that MCC formation requires a high strain rate ($\geqslant 1 \times 10^{-16}$ s^{-1}) and a high Moho temperature (≥700 °C; Figure 6a). The symmetric-dome mode occurred at lower strain rates, which did not develop a detachment fault. Although models E1T750 and E1T800 could form an MCC, it took an unrealistic long time (~60 Myr), which disagrees with the observed rapid exhumation feature (~20 Myr) of MCCs in the field. Thus, we conclude that the optimal conditions for MCC formation in the NCC are $\dot{\varepsilon}_{bg} \geqslant 5 \times 10^{-16}$ s^{-1} and $T_{Moho} \geqslant 700$ °C. No detachment fault or strain localization could form if the background strain rate or the Moho temperature lowered. Instead, the symmetric-dome mode developed, as shown in the yellow area of Figure 6a. Finally, a high background extension rate ($>5 \times 10^{-16}$ s^{-1}) and a low Moho temperature (<650 °C) led to the pure-shear mode (Figure 6a).

Figure 6b shows the weakening proof of the three end-member models, as demonstrated by the viscosity reduction index ($I_r = \frac{\eta_{min}}{\eta_{ave}}$, where η_{min} and η_{ave} are the minimum and average viscosities at a depth of 10 km, respectively) versus the extension (change in length divided by the original length). The MCC mode underwent the most strain localization and weakening (19%) when the crust was stretched to 18%. The symmetric-dome mode underwent intermediate strain localization and weakening (8%) when the crust was extended to 9%. Finally, the crust underwent consistent thinning in the pure-shear mode and thus no strain localization or weakening. The viscosity decreased smoothly; therefore, the minimum viscosity proxy weakened by only 2% when the crust was stretched to 33%.

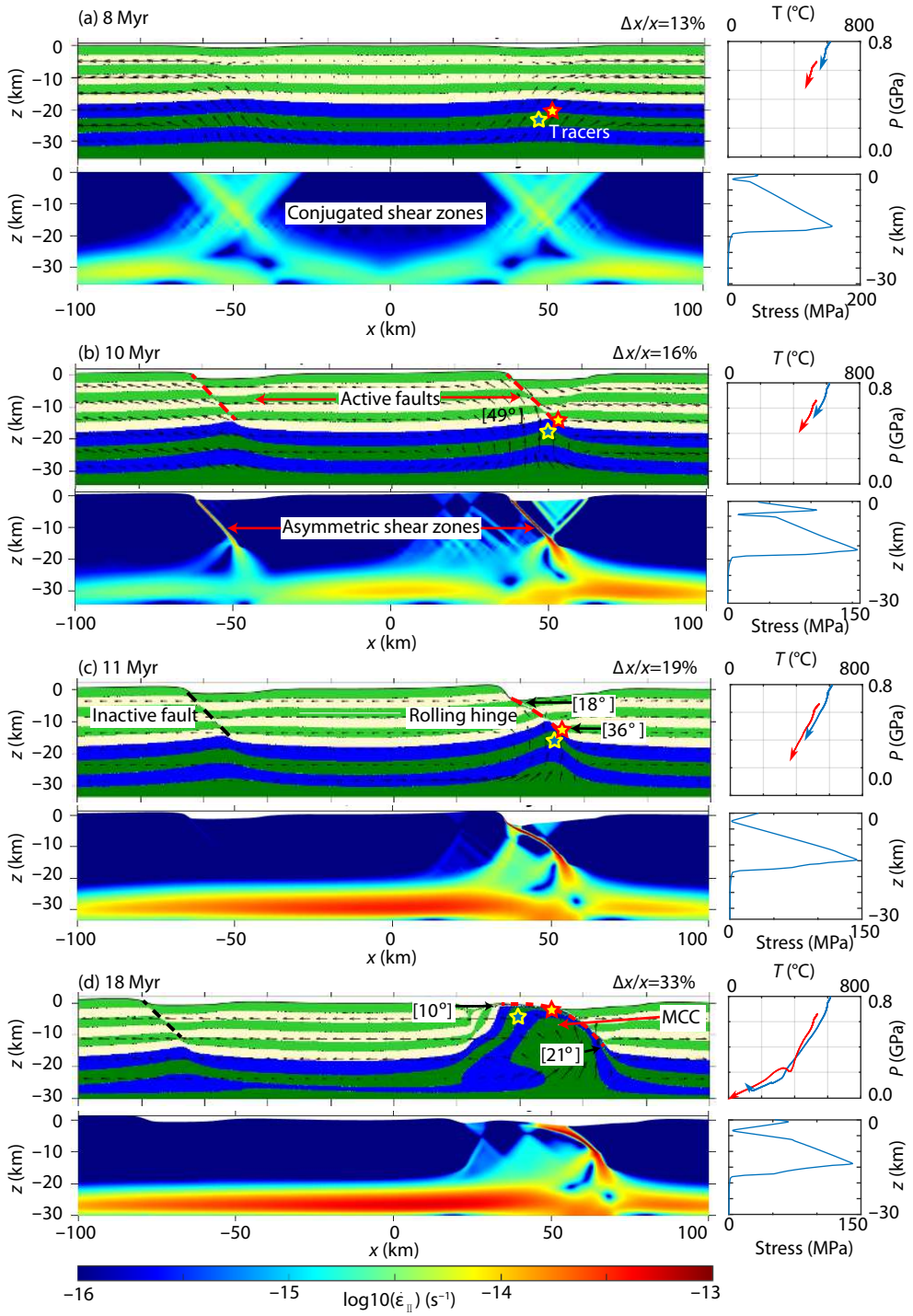

Figure 3. Evolution of the reference MCC mode with $\dot{\varepsilon}_{bg} = 5 \times 10^{-16}$ s^{-1} and T_{Moho} = 750 °C. Stages with total extension at 13% (a), 16% (b), 19% (c), and 33% (d) are shown. In each stage, snapshots of the composition (top left) and strain rate (bottom left) fields, *P-T-t* paths (top right), and strength profile at x = 0 (bottom right) are shown. Red and blue stars in the composition plot indicate locations of the *P-T-t* tracers. The red and black dashed lines indicate active and inactive faults, respectively, with the numbers showing their dipping angles in degrees. Note the decrease of dip angle from 49° to 10° to 21° of the asymmetric shear zone at x = 50 km, showing the rolling hinge mode for MCC formation.

5. Discussion

5.1 Comparison with Observational Data

Figure 7 shows a comparison of *T-t* paths in our models with field data (Lin W and Wei W, 2020). Note that some MCCs could reach a cooling rate of ~50 °C/Myr, such as the Hohhot, Yunmeng Mountain (Chen Y et al., 2014), and Yagan MCCs. In comparison, the slope of model E5T750, the MCC mode (deep blue, ~55 °C/Myr), best fit that of the actual cooling rate of MCCs, such as the Hohhot, Yunmeng Mountain, and Yagan MCCs, whereas the symmetric-dome (~3 °C/Myr) and pure-shear modes (~2 °C/Myr) all experienced slow cooling rates. Therefore, a high strain rate and a high

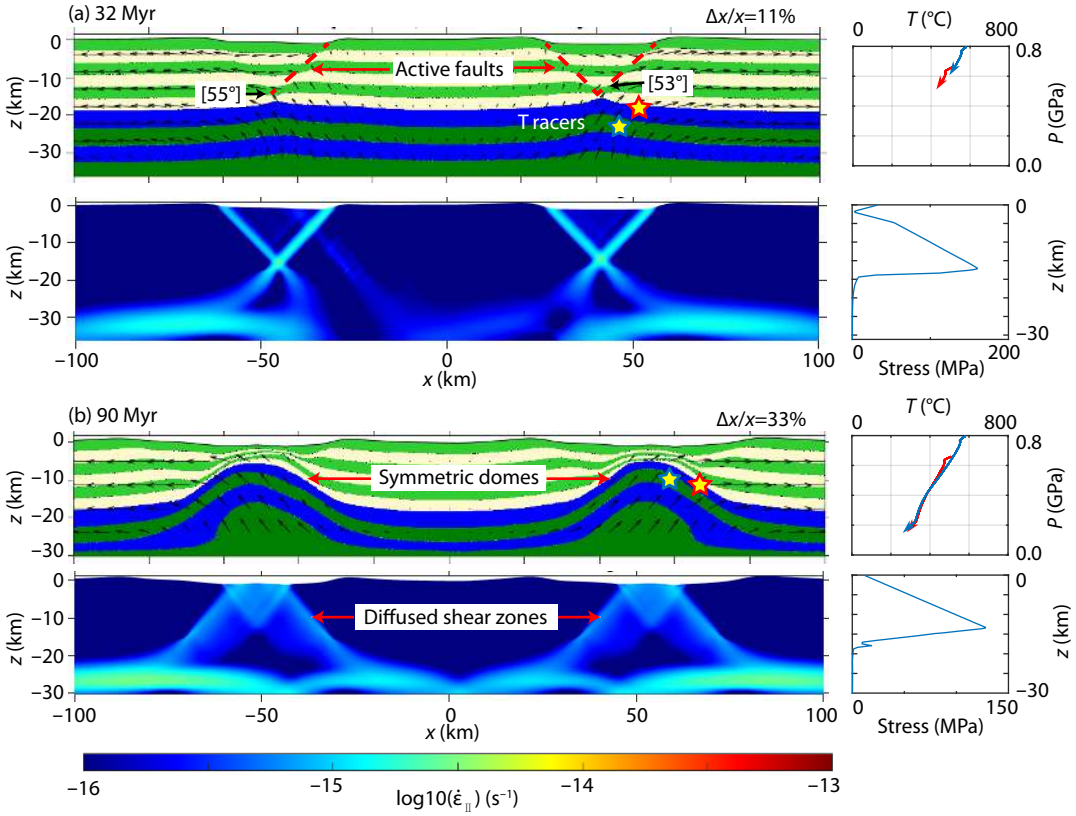

Figure 4. Evolution of the symmetric-dome mode with $\dot{\varepsilon}_{bg}$= 1 × 10^{-16} s^{-1} and T_{Moho} = 700 °C. Stages with total extension at 11% (a) and 33% (b) are shown. See Figure 3 for explanations.

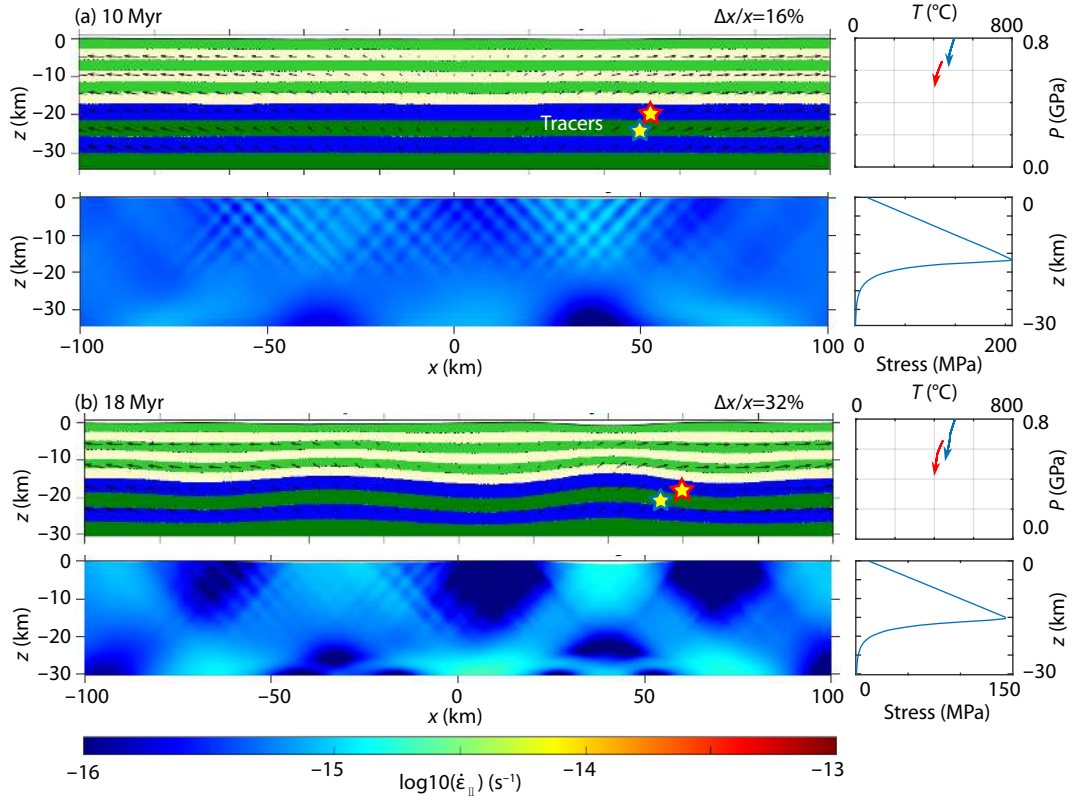

Figure 5. Time evolution of the pure-shear mode, with $\dot{\varepsilon}_{bg}$= 5 × 10^{-16} s^{-1} and T_{Moho} = 600 °C. Stages with extension at 16% (a) and 32% (b) are shown. See Figure 3 for explanations.

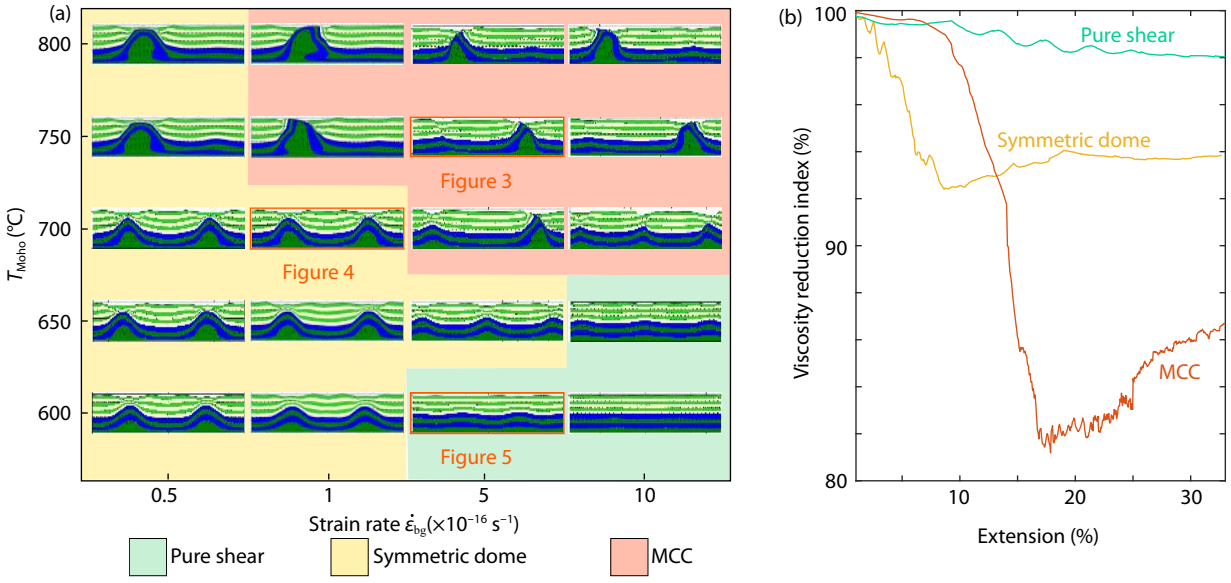

Figure 6. (a) Regime diagram of crustal deformation modes under different background strain rates and Moho temperatures. All models were terminated when the crust was thinned to 30 km (~33% of extension). (b) Evolution of the viscosity reduction index ($I_r = \frac{\eta_{min}}{\eta_{ave}}$, where η_{min} and η_{ave} are the minimum and average viscosities at a depth of 10 km, respectively) of the three end-member models.

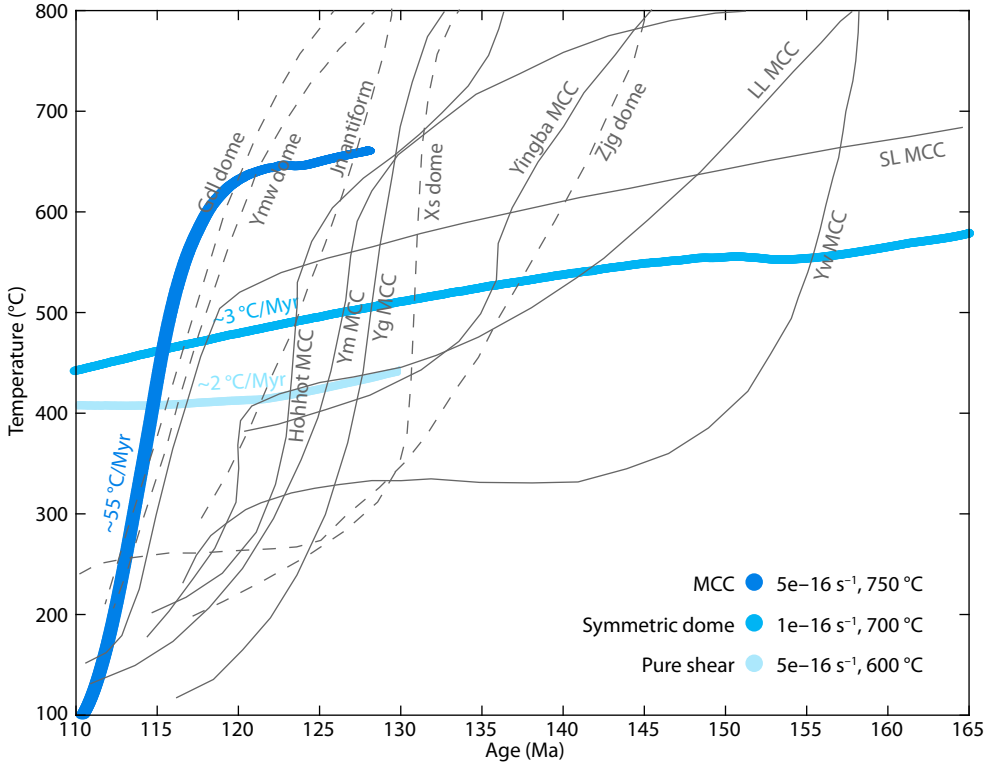

Figure 7. Comparison of cooling paths between end-member models in this study (blue lines) and field data (gray lines) from Lin W and Wei W (2020). Model cooling paths are aligned, assuming their final age is 110 Ma. See Figure 1 for the MCC names and locations.

temperature were the necessary conditions for rapid exhumation. Lacking either one, rapid exhumation failed to develop.

5.2 Thermal State of the Lithosphere in the NCC in the Cretaceous

Using an initial steady-state continental geotherm in our models allowed us to further estimate the thermal state of the lithosphere of the eastern NCC at the start of the extension (Figure 8a). Because the temperature and the heat flux were continuous at all depths in our model, the thermal gradient at the Moho (Equation (9)) equaled the Moho heat flux calculated from the mantle temperature profile. A stable craton with a LAB depth of 200 km

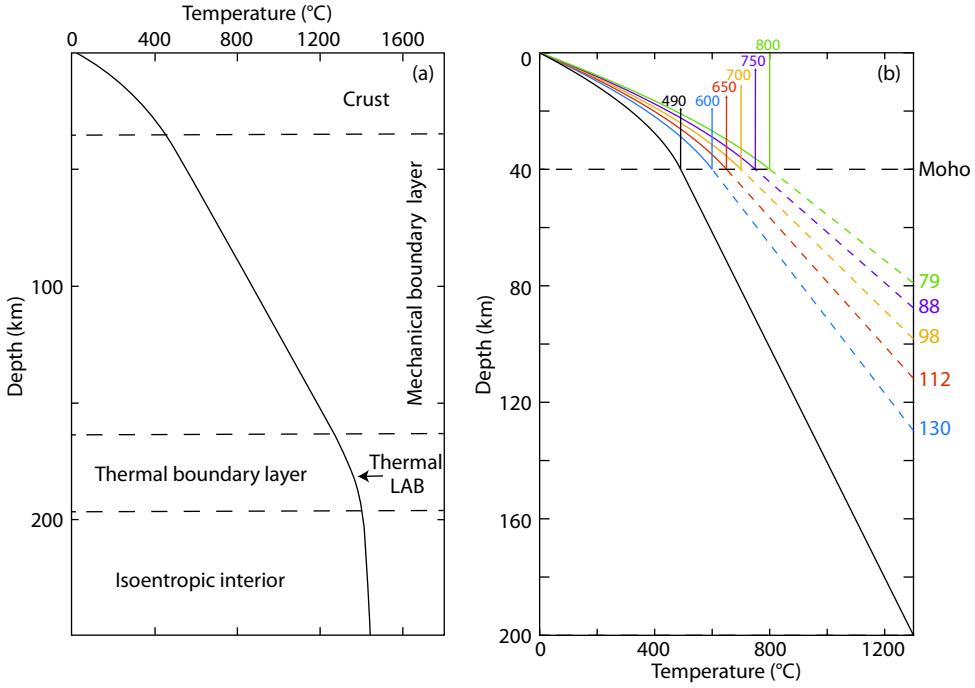

Figure 8. (a) The steady-state thermal structure of the old lithosphere. The corresponding structure for the plate model is shown as a dotted line, visible only in the middle of the thermal boundary layer. The thermal LAB is defined at the middle of the thermal boundary layer. Modified from McKenzie et al. (2005). (b) Depth of the LAB as a function of the Moho temperature, assuming an initial steady-state continental lithosphere geotherm. The horizontal black dashed line denotes the Moho discontinuity. Radioactive heat generation was $H_r = 9 \times 10^{-7}$ W/m^3 in the crust and zero in the mantle lithosphere. The isotherm of 1,300 °C was regarded as the LAB. The colored numbers indicate the LAB depth in kilometers derived from the T_{Moho}, ranging from 600 to 800 °C. The solid black line represents the typical cratonic geotherm with a LAB depth of 200 km.

would require a Moho temperature of 490 °C for the same radioactive heat used in this study. By extrapolating the initial temperature in our models using the thermal gradient at the Moho, we were able to project the LAB depth by using a base lithosphere temperature of 1,300 °C for each model. The minimum Moho temperature (700 °C) required for MCC formation in our models suggests that the depth of the LAB would be shallower than ~100 km (Figure 8b). This is much thinner than the "normal" stable cratonic lithosphere, suggesting that the eastern NCC had thinned prior to the formation of MCCs in the Mesozoic.

5.3 Slab Rollback as a Mechanism of MCC Formation

Analysis of the geometric, kinematic, and chronological data for the MCCs showed that MCCs in the NCC, distributed over a domain of >1,500 km, shared the same extension direction and activity time, implying a common large-scale geodynamic mechanism. Several possible explanations have been proposed: (1) back-arc extension caused by the subduction of the paleo-Pacific plate (Zhu G et al., 2012; Liu JL et al., 2013; Chen Y et al., 2014; Ji M et al., 2015; Zheng JP and Dai HK, 2018; Li YJ et al., 2020); (2) foundering of the lower crust, the mantle lithosphere, or both (Gao S et al., 2004; Lin W and Wang QC, 2006; Lin W and Wei W, 2020); (3) post-orogenic collapse (Coney and Harms, 1984; Lister et al., 1984; Zheng YD et al., 1988; Davis et al., 2002; Darby et al., 2004; Zheng YD and Wang T, 2005; Huet et al., 2011; Wang T et al., 2011; Jolivet et al., 2013); and (4) mantle plume upwelling (Xu YG, 2001).

Delamination of the lower crust, the mantle lithosphere, or both may replace the initial lithosphere with the sublithospheric mantle, leading to a hotter thermal state that favors MCC formation and would explain the widespread volcanism and magmatism. However, the sinking delaminated lower part of the lithosphere tends to develop downwelling of the mantle flow, which induces a convergent horizontal flow and imposes compressional stress on the surface. As shown in our models, MCC formation requires not only a high Moho temperature but also a large extensional strain rate, which is not guaranteed during delamination. Thus, delamination alone is unlikely the dominant mechanism of MCC development.

Post-orogenic gravitational collapse provides a potential mechanism for the required extensional stress field for individual MCCs. Because gravitational collapse forces are largest along the direction of the steepest topographic change, the extension direction is expected to be perpendicular to the strike of the orogen. This is, however, inconsistent with field observations that the widespread MCCs in the NCC exhibit a uniform northwest-southeast extension direction, unrelated to the strikes of the orogens (Figure 1a). Moreover, MCCs in the NCC occur at several orogens forming at a similar age. It is difficult to explain why these MCCs were developed almost simultaneously across the entire domain by post-orogenic gravitational collapse.

The mantle plume hypothesis is another mechanism that could induce high geotherm and extensional stresses. However, earlier

studies showed that a plume generates a radial pattern when it spreads out like a mushroom cloud (Xu YG, 2001), which cannot explain the uniform extension direction of MCCs in the NCC. It is also unlikely that multiple plumes arrived simultaneously over a broad domain of >1,800 km.

None of these three mechanisms alone can be the dominant driving mechanism for MCC development in the NCC. The simultaneous occurrence of MCCs implies that a single large-scale tectonic event might have controlled them. We suggest that far-field extensional stress resulting from trench retreat of the paleo-Pacific slab is a plausible mechanism for MCC formation and magmatism during the Mesozoic and a reasonable driving force for destruction of the NCC. The sinking of subducting slab may exert additional mantle drag force through convection (Lu G et al., 2021) that enables extension far away from the trench. The uniform extension direction of MCCs, which is perpendicular to the strike of the paleo-Pacific subduction trench, is consistent with the potential retreat direction. On the basis of our results, the minimum background strain rate for an MCC to form is 5×10^{-16} s^{-1}. Assuming that this strain rate is the average value over the extensional domain from the trench to the westernmost Hohhot MCC, which is 1,800 km wide (Li YJ et al., 2020), we obtained a minimum trench retreat velocity of 2.8 cm/yr if the interior of the Eurasia plate is stationary. This estimate is consistent with the mean speed of global slab retreat of 1.3–1.5 cm/yr by Schellart et al. (2008) and comparable in the order of magnitude with the value (8.8 cm/yr) proposed by Zhu RX et al. (2015).

6. Conclusions

We used 2-D thermomechanical models to simulate the formation of an MCC with an initial steady-state continental geotherm. Our models show that crustal deformation under extension exhibits three distinct modes: MCC, symmetric-dome, and pure-shear. Formation of an MCC requires a high Moho temperature (T_{Moho} ≥700 °C) and $\dot{\varepsilon}_{\mathrm{bg}} \geqslant 5 \times 10^{-16}$ s^{-1}. Assuming that the pre-extension geotherm is in a steady state, we estimate that the LAB depth at the start of the extension was ~100 km or shallower. We propose that far-field stress induced by trench retreat of the paleo-Pacific plate resulted in the lithospheric destruction that was a prerequisite for the later formation of MCCs with the same extension direction (northwest-southeast) in the NCC. The extensional strain rate threshold required for MCC formation (5×10^{-16} s^{-1}) may place a new constraint on the minimum trench retreat velocity of 2.8 cm/yr.

Acknowledgments

The code MILAMIN_VEP was developed by Boris Kaus at the University of Mainz, Germany. We thank Wei Leng (Editor) and two anonymous reviewers for their constructive comments that significantly improved the manuscript. We also acknowledge helpful discussions with Kun Wang and Zimu Wu, as well as the computing time granted on Wukong. This research is supported by the National Natural Science Foundation of China (Grant No. 41774112).

References

Anderson, E. M. (1951). *The Dynamics of Faulting and Dyke Formation with Applications to Britain* (2nd ed). Edinburgh: Oliver and Boyd.

Axen, G. J., and Hartley, J. M. (1997). Field tests of rolling hinges: Existence, mechanical types, and implications for extensional tectonics. *J. Geophys. Res.: Solid Earth*, *102*(B9), 20515–20537. https://doi.org/10.1029/97JB01355

Bao, X. W., Song, X. D., and Li, J. T. (2015). High-resolution lithospheric structure beneath Mainland China from ambient noise and earthquake surface-wave tomography. *Earth Planet. Sci. Lett.*, *417*, 132–141. https://doi.org/10.1016/j.epsl.2015.02.024

Brun, J. P. (1999). Narrow rifts versus wide rifts: Inferences for the mechanics of rifting from laboratory experiments. *Philos. Trans. Roy. Soc. Lond. A: Math. Phys. Eng. Sci.*, *357*(1753), 695–712. https://doi.org/10.1098/rsta.1999.0349

Brun, J. P., Sokoutis, D., and van den Driessche, J. (1994). Analogue modeling of detachment fault systems and core complexes. *Geology*, *22*(4), 319–322. https://doi.org/10.1130/0091-7613(1994)022<0319:AMODFS>2.3.CO;2

Brun, J. P., Sokoutis, D., Tirel, C., Gueydan, F., van den Driessche, J., and Beslier, M. O. (2018). Crustal versus mantle core complexes. *Tectonophysics*, *746*, 22–45. https://doi.org/10.1016/j.tecto.2017.09.017

Buck, W. R. (1991). Modes of continental lithospheric extension. *J. Geophys. Res.: Solid Earth*, *96*(B12), 20161–20178. https://doi.org/10.1029/91JB01485

Chen, L., Zheng, T. Y., and Xu, W. W. (2006). A thinned lithospheric image of the Tanlu Fault Zone, eastern China: Constructed from wave equation based receiver function migration. *J. Geophys. Res.: Solid Earth*, *111*(B9), B09312. https://doi.org/10.1029/2005JB003974

Chen, L. (2010). Concordant structural variations from the surface to the base of the upper mantle in the North China Craton and its tectonic implications. *Lithos*, *120*(1-2), 96–115. https://doi.org/10.1016/j.lithos.2009.12.007

Chen, Y., Zhu, G., Jiang, D. Z., and Lin, S. Z. (2014). Deformation characteristics and formation mechanism of the Yunmengshan metamorphic core complex. *Chin. Sci. Bull.*, *59*(20), 2419–2438. https://doi.org/10.1007/s11434-014-0167-z

Coney, P. J., (1980). Cordilleran metamorphic core complexes: An overview. In M. D. Crittenden Jr., et al. (Eds.), *Cordilleran Metamorphic Core Complexes* (Vol. 153, pp. 7–31). Boulder: GSA. https://doi.org/10.1130/MEM153-p7

Coney, P. J., and Harms, T. A. (1984). Cordilleran metamorphic core complexes: Cenozoic extensional relics of Mesozoic compression. *Geology*, *12*(9), 550–554. https://doi.org/10.1130/0091-7613(1984)12<550:CMCCCE>2.0.CO;2

Darby, B. J., Davis, G. A., Zhang, X. H., Wu, F. Y., Wilde, S., and Yang, J. H. (2004). The newly discovered Waziyu metamorphic core complex, Yiwulü Shan, western Liaoning province, Northwest China. *Earth Sci. Front.*, *11*(3), 145–156.

Davis, G. A., Darby, B. J., Zheng, Y. D., and Spell, T. L. (2002). Geometric and temporal evolution of an extensional detachment fault, Hohhot metamorphic core complex, Inner Mongolia, China. *Geology*, *30*(11), 1003–1006. https://doi.org/10.1130/0091-7613(2002)030<1003:GATEOA>2.0.CO;2

Davis, G. H., and Coney, P. J. (1979). Geologic development of the Cordilleran metamorphic core complexes. *Geology*, *7*(3), 120–124. https://doi.org/10.1130/0091-7613(1979)7<120:GDOTCM>2.0.CO;2

Gao, S., Rudnick, R. L., Yuan, H. L., Liu, X. M., Liu, Y. S., Xu, W. L., Ling, W. L., Ayers, J., Wang, X. C., and Wang, Q. H. (2004). Recycling lower continental crust in the North China craton. *Nature*, *432*(7019), 892–897. https://doi.org/10.1038/nature03162

Gessner, K., Wijns, C., and Moresi, L. (2007). Significance of strain localization in the lower crust for structural evolution and thermal history of metamorphic core complexes. *Tectonics*, *26*(2), TC2012. https://doi.org/10.1029/2004TC001768

Griffin, W. L., Zhang, A. D., O'Reilly, S. Y., and Ryan, C. G. (1998). Phanerozoic evolution of the lithosphere beneath the Sino-Korean craton. In M. F. J. Flower, et al. (Eds.), *Mantle Dynamics and Plate Interactions in East Asia* (pp. 107–126). Washington, DC: American Geophysical Union.

Hu, S. B., He, L. J., and Wang, J. Y. (2000). Heat flow in the continental area of China: A new data set. *Earth Planet. Sci. Lett.*, *179*(2), 407–419. https://doi.org/10.1016/S0012-821X(00)00126-6

Huet, B., Le Pourhiet, L., Labrousse, L., Burov, E., and Jolivet, L. (2011). Post-orogenic extension and metamorphic core complexes in a heterogeneous

crust: The role of crustal layering inherited from collision. Application to the Cyclades (Aegean domain). *Geophys. J. Int.*, *184*(2), 611–625. https://doi.org/10.1111/j.1365-246X.2010.04849.x

Ji, M., Liu, J. L., Hu, L., Shen, L., and Guan, H. M. (2015). Evolving magma sources during continental lithospheric extension: Insights from the Liaonan metamorphic core complex, eastern North China craton. *Tectonophysics*, *647–648*, 48–62. https://doi.org/10.1016/j.tecto.2015.01.023

Jolivet, L., Faccenna, C., Huet, B., Labrousse, L., Le Pourhiet, L., Lacombe, O., Lecomte, E., Burov, E., Denèle, Y., … Driussi, O. (2013). Aegean tectonics: Strain localisation, slab tearing and trench retreat. *Tectonophysics*, *597–598*, 1–33. https://doi.org/10.1016/j.tecto.2012.06.011

Kaus, B. J. P. (2010). Factors that control the angle of shear bands in geodynamic numerical models of brittle deformation. *Tectonophysics*, *484*(1-4), 36–47. https://doi.org/10.1016/j.tecto.2009.08.042

Kaus, B. J. P., Mühlhaus, H., and May, D. A. (2010). A stabilization algorithm for geodynamic numerical simulations with a free surface. *Phys. Earth Planet. Inter.*, *181*(1-2), 12–20. https://doi.org/10.1016/j.pepi.2010.04.007

Lavier, L. L., Buck, W. R., and Poliakov, A. N. B. (1999). Self-consistent rolling-hinge model for the evolution of large-offset low-angle normal faults. *Geology*, *27*(12), 1127–1130. https://doi.org/10.1130/0091-7613(1999)027<1127:SCRHMF>2.3.CO;2

Lavier, L. L., Buck, W. R., and Poliakov, A. N. B. (2000). Factors controlling normal fault offset in an ideal brittle layer. *J. Geophys. Res.: Solid Earth*, *105*(B10), 23431–23442. https://doi.org/10.1029/2000jb900108

Lavier, L. L., and Buck, W. R. (2002). Half graben versus large-offset low-angle normal fault: Importance of keeping cool during normal faulting. *J. Geophys. Res.: Solid Earth*, *107*(B6), ETG 8-1-ETG 8-13. https://doi.org/10.1029/2001jb000513

Le Pourhiet, L., Huet, B., May, D. A., Labrousse, L., and Jolivet, L. (2012). Kinematic interpretation of the 3D shapes of metamorphic core complexes. *Geochem. Geophys. Geosyst.*, *13*(9), Q09002. https://doi.org/10.1029/2012GC004271

Li, Y. J., Zhu, G., Su, N., Xiao, S. Y., Zhang, S., Liu, C., Xie, C. L., Yin, H., and Wu, X. D. (2020). The Xiaoqinling metamorphic core complex: A record of Early Cretaceous backarc extension along the southern part of the North China Craton. *GSA Bull.*, *132*(3-4), 617–637. https://doi.org/10.1130/B35261.1

Lin, W., and Wang, Q. C. (2006). Late Mesozoic extensional tectonics in the North China block: A crustal response to subcontinental mantle removal. *Bull. Soc. geol. France*, *177*(6), 287–297. https://doi.org/10.2113/gssgfbull.177.6.287

Lin, W., and Wei, W. (2020). Late Mesozoic extensional tectonics in the North China Craton and its adjacent regions: A review and synthesis. *Int. Geol. Rev.*, *62*(7-8), 811–839. https://doi.org/10.1080/00206814.2018.1477073

Lister, G. S., Banga, G., and Feenstra, A. (1984). Metamorphic core complexes of Cordilleran type in the Cyclades, Aegean Sea, Greece. *Geology*, *12*(4), 221–225. https://doi.org/10.1130/0091-7613(1984)12<221:MCCOCT>2.0.CO;2

Lister, G. S., and Davis, G. A. (1989). The origin of metamorphic core complexes and detachment faults formed during Tertiary continental extension in the northern Colorado River region, U. S. A. *J. Struct. Geol.*, *11*(1-2), 65–94. https://doi.org/10.1016/0191-8141(89)90036-9

Liu, D. Y., Nutman, A. P., Compston, W., Wu, J. S., and Shen, Q. H. (1992). Remnants of ≥3800 Ma crust in the Chinese part of the Sino-Korean craton. *Geology*, *20*(4), 339–342. https://doi.org/10.1130/0091-7613(1992)020<0339:ROMCIT>2.3.CO;2

Liu, J. L., Davis, G. A., Lin, Z. Y., and Wu, F. Y. (2005). The Liaonan metamorphic core complex, Southeastern Liaoning Province, North China: A likely contributor to Cretaceous rotation of Eastern Liaoning, Korea and contiguous areas. *Tectonophysics*, *407*(1-2), 65–80. https://doi.org/10.1016/j.tecto.2005.07.001

Liu, J. L., Shen, L., Ji, M., Guan, H. M., Zhang, Z. C., and Zhao, Z. D. (2013). The Liaonan/Wanfu metamorphic core complexes in the Liaodong Peninsula: Two stages of exhumation and constraints on the destruction of the North China Craton. *Tectonics*, *32*(5), 1121–1141. https://doi.org/10.1002/tect.20064

Lu, G., Zhao, L., Zheng, T. Y., Wang, K., and Yang, J. F. (2016). Determining the key conditions for the formation of metamorphic core complexes by geodynamic modeling and insights into the destruction of North China Craton. *Sci. China Earth Sci.*, *59*(9), 1873–1884. https://doi.org/10.1007/s11430-015-5407-5

Lu, G., Zhao, L., Chen, L., Wan, B. and Wu, F. Y. (2021). Reviewing subduction initiation and the origin of plate tectonics: What do we learn from present-day Earth?. *Earth Planet. Phys.*, *5*(2), 123–140. https://doi.org/10.26464/epp2021014

McKenzie, D., Jackson, J., and Priestley, K. (2005). Thermal structure of oceanic and continental lithosphere. *Earth Planet. Sci. Lett.*, *233*(3-4), 337–349. https://doi.org/10.1016/j.epsl.2005.02.005

Menzies, M., Xu, Y. G., Zhang, H. F., and Fan, W. M. (2007). Integration of geology, geophysics and geochemistry: A key to understanding the North China Craton. *Lithos*, *96*(1-2), 1–21. https://doi.org/10.1016/j.lithos.2006.09.008

Platt, J. P., Behr, W. M., and Cooper, F. J. (2015). Metamorphic core complexes: Windows into the mechanics and rheology of the crust. *J. Geol. Soc.*, *172*(1), 9–27. https://doi.org/10.1144/jgs2014-036

Püthe, C., and Gerya, T. (2014). Dependence of mid-ocean ridge morphology on spreading rate in numerical 3-D models. *Gondwana Res.*, *25*(1), 270–283. https://doi.org/10.1016/j.gr.2013.04.005

Rey, P. F., Teyssier, C., and Whitney, D. L. (2009a). Extension rates, crustal melting, and core complex dynamics. *Geology*, *37*(5), 391–394. https://doi.org/10.1130/G25460A.1

Rey, P. F., Teyssier, C., and Whitney, D. L. (2009b). The role of partial melting and extensional strain rates in the development of metamorphic core complexes. *Tectonophysics*, *477*(3-4), 135–144. https://doi.org/10.1016/j.tecto.2009.03.010

Schellart, W. P., Stegman, D. R., and Freeman, J. (2008). Global trench migration velocities and slab migration induced upper mantle volume fluxes: Constraints to find an Earth reference frame based on minimizing viscous dissipation. *Earth-Sci. Rev.*, *88*(1-2), 118–144. https://doi.org/10.1016/j.earscirev.2008.01.005

Schenker, F. L., Gerya, T., and Burg, J. P. (2012). Bimodal behavior of extended continental lithosphere: Modeling insight and application to thermal history of migmatitic core complexes. *Tectonophysics*, *579*, 88–103. https://doi.org/10.1016/j.tecto.2012.07.002

Schmalholz, S. M., Kaus, B. J. P., and Burg, J. P. (2009). Stress-strength relationship in the lithosphere during continental collision. *Geology*, *37*(9), 775–778. https://doi.org/10.1130/G25678A.1

Thielmann, M., and Kaus, B. J. P. (2012). Shear heating induced lithospheric-scale localization: Does it result in subduction?. *Earth Planet. Sci. Lett.*, *359–360*, 1–13. https://doi.org/10.1016/j.epsl.2012.10.002

Tirel, C., Brun, J. P., and Burov, E. (2004). Thermomechanical modeling of extensional gneiss domes. In D. L. Whitney, et al. (Eds.), *Gneiss Domes in Orogeny* (Vol. 380, pp. 67–78). Boulder: GSA. https://doi.org/10.1130/0-8137-2380-9.67

Tirel, C., Brun, J. P., and Sokoutis, D. (2006). Extension of thickened and hot lithospheres: Inferences from laboratory modeling. *Tectonics*, *25*(1), TC1005. https://doi.org/10.1029/2005TC001804

Tirel, C., Brun, J. P., and Burov, E. (2008). Dynamics and structural development of metamorphic core complexes. *J. Geophys. Res.: Solid Earth*, *113*(4), B04403. https://doi.org/10.1029/2005JB003694

Wang, H. Z., and Mo, X. X. (1995). An outline of the tectonic evolution of China. *Episodes*, *18*(1-2), 6–16. https://doi.org/10.18814/epiiugs/1995/v18i1.2/003

Wang, K., Burov, E., Gumiaux, C., Chen, Y., Lu, G., Mezri, L., and Zhao, L. (2015). Formation of metamorphic core complexes in non-over-thickened continental crust: A case study of Liaodong Peninsula (East Asia). *Lithos*, *238*, 86–100. https://doi.org/10.1016/j.lithos.2015.09.023

Wang, T., Zheng, Y. D., Zhang, J. J., Zeng, L. S., Donskaya, T., Guo, L., and Li, J. B. (2011). Pattern and kinematic polarity of late Mesozoic extension in continental NE Asia: Perspectives from metamorphic core complexes. *Tectonics*, *30*(6), TC6007. https://doi.org/10.1029/2011TC002896

Wei, Z. G., Chen, L., Jiang, M. M., and Ling, Y. (2015). Lithospheric structure

beneath the central and western North China Craton and the adjacent Qilian orogenic belt from Rayleigh wave dispersion analysis. *Tectonophysics*, *646*, 130–140. https://doi.org/10.1016/j.tecto.2015.02.008

Wernicke, B. (1981). Low-angle normal faults in the Basin and Range Province: Nappe tectonics in an extending orogen. *Nature*, *291*(5817), 645–648. https://doi.org/10.1038/291645a0

Whitney, D. L., Teyssier, C., Rey, P. F., and Buck, W. R. (2013). Continental and oceanic core complexes. *GSA Bull.*, *125*(3-4), 273–298. https://doi.org/10.1130/B30754.1

Wijns, C., Weinberg, R., Gessner, K., and Moresi, L. (2005). Mode of crustal extension determined by rheological layering. *Earth Planet. Sci. Lett.*, *236*(1-2), 120–134. https://doi.org/10.1016/j.epsl.2005.05.030

Wu, F. Y., Xu, Y. G., Gao, S., and Zheng, J. P. (2008). Lithospheric thinning and destruction of the North China Craton. *Acta Petrol. Sin.* (*in Chinese*), *24*(6), 1145–1174.

Wu, F. Y., Yang, J. H., Xu, Y. G., Wilde, S. A., and Walker, R. J. (2019). Destruction of the north China craton in the Mesozoic. *Annu. Rev. Earth Planet. Sci.*, *47*(1), 173–195. https://doi.org/10.1146/annurev-earth-053018-060342

Wu, G. L., Lavier, L. L., and Choi, E. (2015). Modes of continental extension in a crustal wedge. *Earth Planet. Sci. Lett.*, *421*, 89–97. https://doi.org/10.1016/j.epsl.2015.04.005

Wu, G. L., and Lavier, L. L. (2016). The effects of lower crustal strength and preexisting midcrustal shear zones on the formation of continental core complexes and low-angle normal faults. *Tectonics*, *35*(9), 2195–2214. https://doi.org/10.1002/2016TC004245

Wu, X. D., Zhu, G., Yin, H., Su, N., Lu, Y. C., Zhang, S., and Xie, C. L. (2020). Origin of low-angle ductile/brittle detachments: Examples from the cretaceous Linglong metamorphic core complex in eastern China. *Tectonics*, *39*(9), e2020TC006132. https://doi.org/10.1029/2020TC006132

Xia, B., Thybo, H., and Artemieva, I. M. (2017). Seismic crustal structure of the North China Craton and surrounding area: Synthesis and analysis. *J. Geophys. Res.: Solid Earth*, *122*(7), 5181–5207. https://doi.org/10.1002/2016JB013848

Xu, Y. G. (2001). Thermo-tectonic destruction of the archaean lithospheric keel beneath the Sino-Korean Craton in China: Evidence, timing and mechanism. *Phys. Chem. Earth A*, *26*(9-10), 747–757. https://doi.org/10.1016/S1464-1895(01)00124-7

Zhang, B. L., Zhu, G., Jiang, D. Z., Li, C. C., and Chen, Y. (2012). Evolution of the Yiwulushan metamorphic core complex from distributed to localized deformation and its tectonic implications. *Tectonics*, *31*(4), TC4018. https://doi.org/10.1029/2012TC003104

Zhang, J. J., and Zheng, Y. D. (1999). Multistage extension and age dating of the Xiaoqinling metamorphic core complex, Central China. *Acta Geol. Sin.* (*Engl. Ed.*), *73*(2), 139–147. https://doi.org/10.1111/j.1755-6724.1999.tb00821.x

Zhao, G. C., Sun, M., Wilde, S. A., and Li, S. Z. (2005). Late Archean to Paleoproterozoic evolution of the North China Craton: Key issues revisited. *Precambrian Res.*, *136*(2), 177–202. https://doi.org/10.1016/j.precamres.2004.10.002

Zheng, J. P., and Dai, H. K. (2018). Subduction and retreating of the western Pacific plate resulted in lithospheric mantle replacement and coupled basin-mountain respond in the North China Craton. *Sci. China Earth Sci.*, *61*(4), 406–424. https://doi.org/10.1007/s11430-017-9166-8

Zheng, T. Y., Chen, L., Zhao, L., Xu, W. W., and Zhu, R. X. (2006). Crust-mantle structure difference across the gravity gradient zone in North China Craton: Seismic image of the thinned continental crust. *Phys. Earth Planet. Inter.*, *159*(1-2), 43–58. https://doi.org/10.1016/j.pepi.2006.05.004

Zheng, T. Y., Duan, Y. H., Xu, W. W., and Ai, Y. S. (2017). A seismic model for crustal structure in North China Craton. *Earth Planet. Phys.*, *1*, 26–34. https://doi.org/10.26464/epp2017004

Zheng, Y. D., Wang, Y. F., Liu, R., and Shao, J. A. (1988). Sliding-thrusting tectonics caused by thermal uplift in the Yunmeng Mountains, Beijing, China. *J. Struct. Geol.*, *10*(2), 135–144. https://doi.org/10.1016/0191-8141(88)90111-3

Zheng, Y. D., and Wang, T. (2005). Kinematics and dynamics of the Mesozoic orogeny and late-orogenic extensional collapse in the Sino-Mongolian border areas. *Sci. China Earth Sci.*, *48*(7), 849–862. https://doi.org/10.1360/03yd0552

Zhu, G., Jiang, D. Z., Zhang, B. L., and Chen, Y. (2012). Destruction of the eastern North China Craton in a backarc setting: Evidence from crustal deformation kinematics. *Gondwana Res.*, *22*(1), 86–103. https://doi.org/10.1016/j.gr.2011.08.005

Zhu, R. X., and Zheng, T. Y. (2009). Destruction geodynamics of the North China craton and its Paleoproterozoic plate tectonics. *Chin. Sci. Bull.*, *54*(19), 3354–3366. https://doi.org/10.1007/s11434-009-0451-5

Zhu, R. X., Chen, L., Wu, F. Y., and Liu, J. L. (2011). Timing, scale and mechanism of the destruction of the North China Craton. *Sci. China Earth Sci.*, *54*(6), 789–797. https://doi.org/10.1007/s11430-011-4203-4

Zhu, R. X., Fan, H. R., Li, J. W., Meng, Q. R., Li, S. R., and Zeng, Q. D. (2015). Decratonic gold deposits. *Sci. China Earth Sci.*, *58*(9), 1523–1537. https://doi.org/10.1007/s11430-015-5139-x

Zhu, R. X., and Xu, Y. G. (2019). The subduction of the west Pacific plate and the destruction of the North China Craton. *Sci. China Earth Sci.*, *62*(9), 1340–1350. https://doi.org/10.1007/s11430-018-9356-y

Zhu, R. X., Zhou, Z. H., and Meng, Q. R. (2020). Destruction of the North China Craton and its influence on surface geology and terrestrial biotas. *Chin. Sci. Bull.*, *65*(27), 2954–2965. https://doi.org/10.1360/TB-2020-0219